Paleoceanography and Paleoclimatology

RESEARCH ARTICLE
10.1029/2020PA004159

Key Points:

- We demonstrate that I-type cosmic spherules can be used to determine the isotope composition of air

Correspondence to:
A. Pack,
apack@uni-goettingen.de

Citation:
Fischer, M. B., Oeser, M., Weyer, S., Folco, L., Peters, S. T. M., Zahnow, F., & Pack, A. (2021). I-type cosmic spherules as proxy for the $\Delta'^{17}O$ of the atmosphere—A calibration with quaternary air. *Paleoceanography and Paleoclimatology*, *36*, e2020PA004159. https://doi.org/10.1029/2020PA004159

Received 30 OCT 2020
Accepted 10 FEB 2021

I-Type Cosmic Spherules as Proxy for the $\Delta'^{17}O$ of the Atmosphere—A Calibration With Quaternary Air

Meike B. Fischer[1,2], Martin Oeser[3], Stefan Weyer[3], Luigi Folco[4,5], Stefan T. M. Peters[1], Fabian Zahnow[1], and Andreas Pack[1]

[1]Geowissenschaftliches Zentrum, Universität Göttingen, Göttingen, Germany, [2]Planets and Comets Department, Max Planck Institute for Solar System Research, Göttingen, Germany, [3]Institut für Mineralogie, Universität Hannover, Hannover, Germany, [4]Dipartimento di Scienze della Terra, Università di Pisa, Pisa, Italy, [5]CISUP - Centro per l'Integrazione della Strumentazione dell'Università di Pisa, Pisa, Italy

Abstract Remnants of shooting stars are preserved in form of cosmic spherules in ice and sediments. The extraterrestrial material is heated and melted upon atmospheric entry and is collected at the Earth's surface as cosmic spherules. A fraction of cosmic spherules (I-type cosmic spherules) sources from extraterrestrial Fe,Ni metal. These metal particles melt and become oxidized in the atmosphere. The oxygen in the resulting oxides (magnetite, wüstite) sources entirely from the atmosphere. Here, we demonstrate that I-type cosmic spherules can be used to reconstruct the triple oxygen isotope anomaly of the past atmosphere, which provides information on the gross primary productivity and/or paleo-CO_2 levels. We present a calibration of the proxy using Antarctic cosmic spherules. We further introduce $\Delta'^{56}Fe$ and demonstrate that triple iron isotopes can be used to obtain information about the underlying fractionation mechanism (e.g., kinetic vs. equilibrium fractionation).

1. Introduction

The isotope composition of atmospheric molecular oxygen (O_2) is controlled by mass-dependent fractionation associated with marine and terrestrial photosynthesis, respiration, and mass-independent fractionation associated with the formation of ozone (Thiemens et al., 2012; Young et al., 2014). Because of exotic mass-independent effects associated with stratosphere ozone formation, molecular O_2 is the only indigenous terrestrial component that carries a negative ^{17}O anomaly (Luz et al., 1999). The degree of the anomaly is expressed in form of the $\Delta'^{17}O$ notation (Equation 1).

$$\Delta'^{17}O^{\text{sample}}_{0.528} = \ln\left(\frac{\delta^{17}O^{\text{sample}}_{\text{VSMOW}}}{1{,}000}+1\right) - 1{,}000\times 0.528\ln\left(\frac{\delta^{18}O^{\text{sample}}_{\text{VSMOW}}}{1{,}000}+1\right) \quad (1)$$

No consensus has yet been reached on which slope of the reference line should be chosen. We choose a reference line with a slope of 0.528 in order to have a consistent terminology across disciplines (see discussion, e.g., in Miller & Pack, 2021, Pack & Herwartz, 2014, or Sharp & Wostbrock, 2021). However, any of the definitions of $\Delta'^{17}O$ used in the literature, does not change the interpretation of triple oxygen isotope data. Modern tropospheric O_2 has a composition of $\delta^{18}O = 24‰$ (i.e., the $^{18}O/^{16}O$ ratio is 2.4% higher than in ocean water) and $\Delta'^{17}O = -0.432 \pm 0.010‰$ (Pack et al., 2017; Wostbrock et al., 2020; Yeung et al., 2012; Young et al., 2014). The high $\delta^{18}O$ is due to the preferential uptake of light O_2 during respiration (Dole effect; Dole et al., 1954). The negative anomaly in $\Delta'^{17}O$ of O_2 counter-balances the large positive anomalies of stratospheric O_3 (Heidenreich & Thiemens, 1986; Krankowsky et al., 2000; Lämmerzahl, 2002; Thiemens & Heidenreich, 1983) and stratospheric CO_2 (Boering, 2004; Kawagucci et al., 2008; Lämmerzahl, 2002; Thiemens et al., 1995). Anomalous O_2 is mixed with isotopically normal O_2 from marine and terrestrial photosynthesis. The size of the negative anomaly of O_2 is a direct function of gross primary production (GPP) and atmospheric CO_2 mixing ratio [CO_2]. The close coupling between $\Delta'^{17}O$ of O_2 and [CO_2] and GPP has been verified using $\Delta'^{17}O$ of O_2 and [CO_2] data from ice cores (Blunier et al., 2002; Brandon et al., 2020).

The relation between [CO_2], GPP, and $\Delta'^{17}O$ of air O_2 has been modeled by Young et al. (2014). For modern air O_2, the Young et al. (2014) model predicts a $\Delta'^{17}O$ that is slightly higher than the measured −0.432‰ (average of Pack et al., 2017; Wostbrock et al., 2020; Yeung et al., 2012; and Young et al., 2014). We adjusted

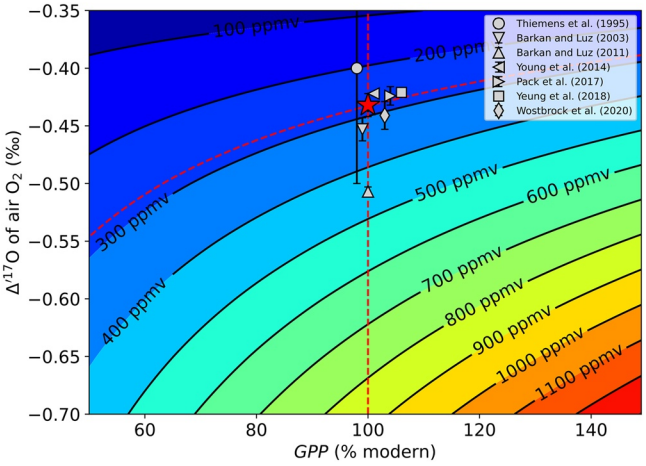

Figure 1. Plot of $\Delta'^{17}O$ versus GPP with $[CO_2]$ isobars from the model of Young et al. (2014). Measured modern air compositions are shown with light gray-filled markers (markers are displaced in GPP for better visibility; Barkan & Luz, 2005, 2011; Pack et al., 2017; Thiemens et al., 1995; Wostbrock et al., 2020; Yeung et al., 2012; Young et al., 2014). The red star indicates the pre-industrial situation (280 ppmv CO_2, $\Delta'^{17}O_{O2} = -0.432‰$).

the $\Delta'^{17}O$ of the Young et al. (2014) model data so that the predicted model value matches the measured $\Delta'^{17}O$ of modern air O_2. (Figure 1). The $[CO_2]$ varies with GPP and $\Delta'^{17}O$ of air O_2 according to Equation 2 (regression parameters in Table 1).

$$\left[CO_2\right] = a_0 \times GPP + a_1 \times GPP^2 + a_2 \times \Delta'^{17}O + a_3 \times \left(\Delta'^{17}O\right)^2 + a_4 \times GPP \times \Delta'^{17}O + a_5 \quad (2)$$

With $[CO_2]$ in ppmv, GPP in percent relative the modern value (= 100%), and $\Delta'^{17}O$ in per mil (‰).

Beyond the past ~0.8 Ma covered by cores from inland ice sheets, no atmospheric O_2 is preserved in the geological record and proxies have been introduced for paleo-$[CO_2]$ reconstruction. A review on the traces of the isotope anomaly of air O_2 in the lithospheric materials has recently been published by Pack (2021). Bao et al. (2008) reconstructed the $\Delta'^{17}O$ of past O_2 by analyzing the triple oxygen isotope composition of Proterozoic sulfates that originated from subaerial pyrite oxidation and hence contained a fraction of oxygen that was derived from air O_2. Pack et al. (2013) and Gehler et al. (2016) used the $\Delta'^{17}O$ of mammal bioapatite to determine $\Delta'^{17}O$ of past O_2 and used this approach for paleo-CO_2 reconstruction for the late Jurassic and across the Paleocene-Eocene transition. Both approaches have the disadvantage that the portions of anomalous atmospheric oxygen in the sulfate or phosphate are difficult to quantify.

Pack et al. (2017) analyzed the oxygen and iron isotope composition of I-type cosmic spherules and demonstrated that the Earth atmosphere is homogenous in $\Delta'^{17}O$ up to ~100 km. I-type cosmic spherules are remnants of shooting stars that formed by atmospheric oxidation of asteroidal Fe,Ni metal. The oxygen isotope composition of these oxide spherules is controlled by the fractionation during the oxidation and the evaporation; both high-*T* processes with kinetically controlled fractionation. The fractionation during evaporation was quantified by Pack et al. (2017) by measurements of the iron isotope composition of the spherules.

Pack et al. (2017) suggested that the oxygen and iron isotope composition of fossil I-type cosmic spherules allows high-resolution reconstruction of paleo-atmospheric $\Delta'^{17}O$. This approach has the advantage over the approaches by Bao et al. (2008) and Pack et al. (2013) and Gehler et al. (2016) that the entire oxygen in I-type cosmic spherules is of atmospheric origin and, high-precision oxygen isotope analyses provided, allows reconstructing the $\Delta'^{17}O$ of past O_2 with unprecedented high resolution. Pack et al. (2017) analyzed the cosmic spherules by means of continuous-flow isotope ratio monitoring with a limited precision in $\Delta'^{17}O$ of ~50 ppm.

In this contribution, we present new high-precision triple oxygen and iron isotope data set of Antarctic I-type cosmic spherules demonstrate that the isotope composition of these spherules reflects the oxygen isotope composition of the atmosphere.

Micrometeorites are cosmic particles, smaller than 2 mm in size, which have survived the hypervelocity impact with the atmosphere (Genge et al., 2008). Each year, about 1,600 metric tons of micrometeorites arrive at the Earth's surface (Suttle & Folco, 2020; Taylor et al., 1998), ranking micrometeorites as the main source of extraterrestrial material (Folco & Cordier, 2015). Spheroidal micrometeorites, which have been completely molten during the atmospheric entry, are called cosmic spherules (Genge et al., 2008). Cosmic spherules that are mainly composed of Fe,Ni oxides and Fe,Ni metal are termed I-type cosmic spherules. They are composed of magnetite (Fe_3O_4), wüstite ($Fe_{0.97}O$), and in some cases kamacite (α-Fe)

Table 1
List of Least-Square Fit Parameters for Equation 2

Parameter	Best fit
a_0	−7.76791005e-00
a_1	4.78666891e-03
a_2	−3.00809661e+02
a_3	−2.88273427e+02
a_4	−2.22194790e+01
a_5	−2.86677885e+01

or taenite (γ-Fe with higher Ni content, Folco & Cordier, 2015; Genge et al., 2008). The atmospheric oxidation of the Fe,Ni metal alloys occurs at altitudes of ~80–115 km. Occasionally a bleb of Fe,Ni metal is preserved during oxidation, though those blebs are often lost during atmospheric entry (Genge, 2016).

I-type cosmic spherules constitute only about 2% of the total budget of micrometeorites (Taylor et al., 2000).

2. Materials and Methods

2.1. Sampling

A total of 18 I-type cosmic spherules were selected from the Transantarctic Mountains collection (Rochette et al., 2008). Sample details are listed in Table 2.

3. Methods

3.1. Sample Characterization

The dimensions of all samples were measured with an Olympus SZ-CTV optical stereo microscope and by 3-D analysis using stacked images applying a Keyence VK-X200 Series microscope. The mass was measured using a Sartorius ME36S microbalance. The densities were calculated from volume and mass with most samples being approximated as spheres. In five cases, sample shapes were approximated as hemispheres. The surfaces and the chemical composition (semiquantitative) were studied using a Leo 1455VP scanning electron microscope with an Oxford Instruments Inca 6901 energy disperse X-ray spectrometer.

3.2. Oxygen Isotopes

Variations in the oxygen isotope ratios ($^{18}O/^{16}O$, $^{17}O/^{16}O$) are expressed in form of the δ-notation (McKinney et al., 1950) relative to the VSMOW standard and in form of the $\Delta'^{17}O$ notation relative to a reference line with slope $\lambda_{RL} = 0.528$ (Equation 1).

Table 2
List of the Analyzed Spherules With Size, Mass, Calculated Density, and Shape Description

Sample	Diameter (μm)	Volume (mm^3)	Mass (mg)	Density (g/cm^3)	Shape
iCS_Vic_01	436 ± 3	0.043 ± 0.005	0.234 ± 0.005	5.4 ± 0.7	Spherical
iCS_Vic_02	548 ± 3	0.086 ± 0.017	0.457 ± 0.005	5.3 ± 1.1	Oval
iCS_Vic_03	574 ± 3	0.099 ± 0.012	0.59 ± 0.005	6.0 ± 0.7	Oval
iCS_Vic_04	491 ± 4	0.062 ± 0.005	0.342 ± 0.005	5.5 ± 0.4	Spherical, void space
iCS_Vic_05	464 ± 2	0.052 ± 0.004	0.278 ± 0.005	5.3 ± 0.4	Spherical
iCS_Vic_06	522 ± 2	0.074 ± 0.003	0.356 ± 0.005	4.8 ± 0.2	Small void space
iCS_Vic_07	437 ± 2	0.044 ± 0.003	0.213 ± 0.005	4.9 ± 0.3	Small void space
iCS_Vic_08	569 ± 2	0.097 ± 0.004	0.424 ± 0.005	4.4 ± 0.2	Big void space
iCS_Vic_09	516 ± 2	0.072 ± 0.005	0.36 ± 0.005	3.9 ± 0.3	Small void space
iCS_Vic_10	411 ± 4	0.036 ± 0.003	0.198 ± 0.005	5.4 ± 0.5	Spherical, void space
iCS_Vic_11	527 ± 1	0.051 ± 0.002	0.251 ± 0.005	4.9 ± 0.2	Hemispherical
iCS_Vic_12	481 ± 2	0.039 ± 0.004	0.212 ± 0.005	5.5 ± 0.6	Hemispherical
iCS_Vic_13	397 ± 3	0.033 ± 0.005	0.192 ± 0.005	5.9 ± 0.8	Big void space
iCS_Vic_14	531 ± 3	0.052 ± 0.005	0.313 ± 0.005	6.0 ± 0.6	Hemispherical
iCS_Vic_15	481 ± 2	0.058 ± 0.002	0.252 ± 0.005	6.5 ± 0.2	Big void space
iCS_Vic_16	510 ± 4	0.046 ± 0.007	0.309 ± 0.005	6.7 ± 0.9	Hemispherical
iCS_Vic_17	545 ± 1	0.057 ± 0.001	0.335 ± 0.005	5.9 ± 0.2	Hemispherical, void space
iCS_Vic_18	452 ± 2	0.0485 ± 0.002	0.241 ± 0.005	5.0 ± 0.3	Small void space

Note. The uncertainties are given as 1σ SD.

The fractionation factor α_{A-B} (Equation 3) describes the fractionation between two reservoirs A and B. Reservoirs A and B may represent two phases in equilibrium or educt and product of a reaction. The triple oxygen isotope fractionation exponent (θ_O, Equation 3) links the fractionation in $^{17}O/^{16}O$ to the fractionation in $^{18}O/^{16}O$ (Equation 3). The value of θ_O varies with the phases in equilibrium, temperature, and fractionation process (Cao & Liu, 2011; Matsuhisa et al., 1978; Young et al., 2002). As a rule, smaller θ_O values are observed for kinetic effects and higher θ_O values are observed for equilibrium processes.

$$\alpha_{A-B}^{17/16} = \left(\alpha_{A-B}^{18/16}\right)^{\theta_O} \quad (3)$$

The triple oxygen isotope compositions were analyzed period between December 2016 and February 2017 by means of BrF_5 laser fluorination (Sharp, 1990). We used San Carlos olivine with $\delta^{17}O_{VSMOW} = 2.656‰$, $\delta^{18}O_{VSMOW} = 5.119‰$, and $\Delta'^{17}O = -0.052‰$ (Pack et al., 2016; Sharp et al., 2016; Wostbrock et al., 2020) as reference point. As further reference materials, we used Campolungo quartz (hydrothermal vein) with $\delta^{18}O_{VSMOW} = 26.68‰$ (Chapligin et al., 2010) and magnetite from a coarse-grained granulite-facies metamorphic banded iron formation from India (Pack & Herwartz, 2014).

The samples were fluorinated in an atmosphere of ~100 mbar BrF_5 using a 50 W CO_2 laser as heat source. The liberated O_2 was cleared from excess oxidation agent, reaction products, and impurities by means of cryogenic separation and gas chromatography. Details of the procedure have been published in Pack et al. (2016). The measurements of the purified O_2 gas were performed with a MAT253 gas source mass spectrometer. One block with 20 cycles was analyzed for each sample or standard with an integration time of 26 s and an idle time of 15 s. The target signal intensity was 5,700 mV. The oxygen blank of the preparation line was <5% even for the smallest samples analyzed in this study ($m_{magnetite} = 0.192$ mg). The minimum sample size for the procedure was determined as ~ 0.038 ml O_2 (~0.18 mg magnetite, blank-to-sample ratio smaller than 5%). All analyses were normalized to the standard San Carlos olivine. The external reproducibility in $\delta^{18}O$ was 0.4‰ and in $\Delta'^{17}O$ 0.02‰ based on replicate measurements of ~0.3 mg standards (San Carlos olivine, Campolungo quartz, magnetite Mt_07113; Table 3).

3.3. Iron Isotope Analyses

Iron isotopes are reported as $\delta^{56}Fe$ and $\delta^{57}Fe$ relative to IRMM-014. The data is reported in the common δ notation as introduced by McKinney et al. (1950) relative to ^{54}Fe. In analogy to oxygen, the triple iron isotope exponent θ_{Fe} relates variations in the three measured iron isotopes (Equation 4).

$$\alpha_{A-B}^{56/54} = \left(\alpha_{A-B}^{57/54}\right)^{\theta_{Fe}} \quad (4)$$

To depict small variations in the iron isotope compositions from a well-correlated relation in the $\ln(\delta^{56}Fe + 1)$ versus $\ln(\delta^{57}Fe + 1)$ space, we introduce (in analogy to oxygen isotopes) the $\Delta'^{56}Fe$ value here (Equation 5).

$$\Delta'^{56}Fe^{sample} = \ln\left(\delta^{57}Fe_{IRMM-014}^{sample} + 1\right) - 0.6780 \cdot \ln\left(\delta^{56}Fe_{IRMM-014}^{sample} + 1\right) \quad (5)$$

In contrast to oxygen, where, for historic reasons, a slope of the reference line of 0.528 has been chosen, for iron, we choose the high-T approximation for equilibrium fractionation for the three iron isotopes of 0.6780 as slope of the reference line for defining $\Delta'^{56}Fe$ (Young et al., 2002). A similar definition has been introduced by Heard et al. (2020) to display small variations in triple iron isotope ratios. Instead of defining $\Delta'^{56}Fe$, they introduced $\varepsilon'^{56}Fe$, which is 10 times $\Delta'^{56}Fe$ as defined in Equation 5.

The iron isotope composition was determined *in situ* by femto-second laser ablation MC-ICP-MS with spot diameters of 50 μm (e.g., Oeser et al., 2014). The I-type cosmic spherules were placed on an 1 in. mount using a carbon light tab in order to allow recovery of remaining material for oxygen isotope measurements. The samples were very small, so that the topographical effect on the aerosol flux in the sample chamber was negligible. The intensities of $^{54}Fe^+$, $^{56}Fe^+$, $^{57}Fe^+$, and $^{52}Cr^+$ (isobaric elemental interference correction of $^{54}Cr^+$ on $^{54}Fe^+$), $^{58}Ni+$, and $^{60}Ni+$ (instrumental mass bias correction) were measured (see Weyrauch et al., 2017). The high resolution mode was chosen, which provides a high signal intensity and avoids the

Table 3
List of Oxygen Isotope Analyses of Standards San Carlos Olivine, Campolungo Quartz, and Magnetite Mt_0701113

Sample	Identifier	$\delta^{17}O$ (‰)	1σ	$\delta^{18}O$ (‰)	1σ	$\Delta'^{17}O$ (‰)	1σ
San Carlos olivine	SC ol_2	2.74	0.20	5.17	0.37	−0.06	0.03
San Carlos olivine	SC ol_4	2.58	0.20	4.87	0.37	−0.06	0.03
San Carlos olivine	SC ol_5	2.58	0.20	4.87	0.37	−0.06	0.03
San Carlos olivine	SC ol_3_3	2.76	0.20	5.22	0.37	−0.04	0.03
San Carlos olivine	SC ol_4_1	2.88	0.20	5.43	0.37	−0.05	0.03
San Carlos olivine	SC ol_4_4	2.60	0.20	4.90	0.37	−0.07	0.03
San Carlos olivine	SC ol_5_3	2.95	0.20	5.57	0.37	−0.04	0.03
San Carlos olivine	SC ol_17	2.56	0.20	4.82	0.37	−0.06	0.03
San Carlos olivine	SC ol_14	2.63	0.20	4.97	0.37	−0.03	0.03
San Carlos olivine	SC ol_21	2.27	0.20	4.29	0.37	−0.01	0.03
San Carlos olivine	SC ol_18	2.84	0.20	5.36	0.37	−0.03	0.03
San Carlos olivine	SC ol_20	2.76	0.20	5.22	0.37	−0.11	0.03
San Carlos olivine	SC ol_2_1	2.94	0.20	5.56	0.37	−0.03	0.03
San Carlos olivine	SC ol_1_1	2.80	0.20	5.29	0.37	−0.04	0.03
San Carlos olivine	SC ol_1_3	3.01	0.20	5.68	0.37	−0.04	0.03
San Carlos olivine	SC ol_2_2	2.87	0.20	5.43	0.37	−0.05	0.03
San Carlos olivine	SC ol_2_4	2.32	0.20	4.38	0.37	−0.05	0.03
Campolungo quartz	Cl qu_18	13.70	0.20	25.98	0.37	−0.03	0.02
Campolungo quartz	Cl qu_19_2	14.22	0.20	26.97	0.37	−0.07	0.02
Campolungo quartz	Cl qu_16	14.01	0.20	26.58	0.37	−0.07	0.02
Campolungo quartz	Cl qu_17	13.88	0.20	26.32	0.37	−0.06	0.02
Campolungo quartz	Cl qu12	14.23	0.20	27.00	0.37	−0.06	0.02
Campolungo quartz	Cl qu_1_3	14.11	0.20	26.77	0.37	−0.05	0.02
Campolungo quartz	Cl qu_2_3	14.22	0.20	26.97	0.37	−0.05	0.02
Campolungo quartz	Cl qu_3_2	14.18	0.20	26.90	0.37	−0.11	0.02
Campolungo quartz	Cl qu_2_1	13.59	0.20	25.77	0.37	−0.07	0.02
Campolungo quartz	Cl qu_2	13.86	0.20	26.29	0.37	−0.04	0.02
Campolungo quartz	Cl qu_4	14.04	0.20	26.64	0.37	−0.06	0.02
Campolungo quartz	Cl qu_5	14.25	0.20	27.03	0.37	−0.02	0.02
Campolungo quartz	Cl qu_6	14.29	0.20	27.11	0.37	−0.04	0.02
Campolungo quartz	Cl qu_12	14.20	0.20	26.93	0.37	−0.07	0.02
Campolungo quartz	Cl qu_4_3	13.89	0.20	26.35	0.37	−0.06	0.02
Campolungo quartz	Cl qu_4_1	14.03	0.20	26.61	0.37	−0.06	0.02
Campolungo quartz	Cl qu_5_1	14.20	0.20	26.93	0.37	−0.10	0.02
Campolungo quartz	Cl qu_4_2	13.86	0.20	26.28	0.37	−0.03	0.02
Campolungo quartz	Cl qu_5_3	14.18	0.20	26.90	0.37	−0.06	0.02
Magnetite	Mt_070113_24	4.81	0.24	9.08	0.45	−0.08	0.02
Magnetite	Mt_070113_20	4.75	0.24	8.97	0.45	−0.10	0.02
Magnetite	Mt_070113_21	4.83	0.24	9.13	0.45	−0.11	0.02
Magnetite	Mt_070113_23	5.34	0.24	10.09	0.45	−0.13	0.02

argon oxide/nitrides interferences by spectral separation ($^{40}Ar^{16}O^+$ on $^{56}Fe^+$, $^{40}Ar^{16}OH^+$ on $^{57}Fe^+$, $^{40}Ar^{14}N^+$ on $^{54}Fe^+$; Oeser et al., 2014; Weyer & Schwieters, 2003). Most I-type cosmic spherules were measured once for ~170 cycles (first 40 cycles background measurement). Samples iCS_Vic_02 and iCS_Vic_03 were analyzed twice. The external reproducibility was $\delta^{56}Fe_{IRMM\text{-}014} = \pm 0.08‰$ (1σ SD) and $\delta^{57}Fe_{IRMM\text{-}014} = \pm 0.14‰$ (1σ SD). Due to the highly correlated errors in $\delta^{56}Fe$ and $\delta^{57}Fe$, the uncertainty in $\Delta'^{56}Fe$ is only 0.03‰ (1σ SD; Table 4).

4. Results

4.1. Morphology

The spheres all show shapes resulting from melting during their entry (Figure 2). Some spherules show indication for the loss of residual metal during the entry (Figures 2f, 2h, 2q2r).

4.2. Isotopic Compositions

4.2.1. Oxygen Isotopes

The oxygen isotope compositions of the studied cosmic spherules are listed in Table 5. Sample iCS_Vic_08 was lost due to a technical problem and was hence not analyzed.

4.3. Iron Isotopes

The iron isotope compositions of the studied cosmic spherules are listed in Table 6.

Table 4
Results of In Situ LA-ICPMS Iron Isotope Measurements on Three Different Grains (500mt02, 250mt02, and 250mt05) of Internal Standard Magnetite Mt_070113 and Puratronic Fe Metal

Grain, spot	$\delta^{56}Fe$ (‰)	1σ	$\delta^{57}Fe$ (‰)	1σ	$\Delta'^{56}Fe$ (‰)	1σ
500mt02_1	0.90	0.08	1.29	0.14	0.03	0.03
500mt02_2	0.71	0.08	0.99	0.14	0.04	0.03
500mt02_3	0.85	0.08	1.19	0.14	0.04	0.03
250mt02_1	0.95	0.08	1.41	0.14	−0.01	0.03
250mt02_2	0.95	0.08	1.47	0.14	−0.05	0.03
250mt05_1	0.85	0.08	1.27	0.14	−0.01	0.03
250mt05_2	0.82	0.08	1.24	0.14	−0.02	0.03
250mt05_3	0.81	0.08	1.25	0.14	−0.04	0.03
Mean	0.86	0.03	1.26	0.05	0.00	0.01
002_Puratronic	0.06	0.05	0.18	0.11	−0.06	0.04
004_Puratronic	0.05	0.05	0.09	0.11	−0.01	0.04
007_Puratronic	0.18	0.05	0.34	0.11	−0.05	0.04
009_Puratronic	0.13	0.05	0.21	0.11	−0.01	0.04
011_Puratronic	0.07	0.05	0.21	0.11	−0.07	0.04
013_Puratronic	0.11	0.05	0.15	0.11	0.01	0.04
015_Puratronic	0.08	0.05	0.10	0.11	0.01	0.04
018_Puratronic	0.03	0.05	0.02	0.11	0.02	0.04
067_Puratronic	0.02	0.05	−0.01	0.11	0.03	0.04
Mean	0.08	0.02	0.14	0.04	−0.02	0.01

Note. Uncertainties are reported as 1σ SD. Because of correlated errors, the uncertainty in $\Delta'^{56}Fe$ is smaller than what is expected from independent errors in $\delta^{56}Fe$ and $\delta^{57}Fe$. For the Cosmic Spherules, we adopt the uncertainty observed for magnetite.

10.1029/2020PA004159

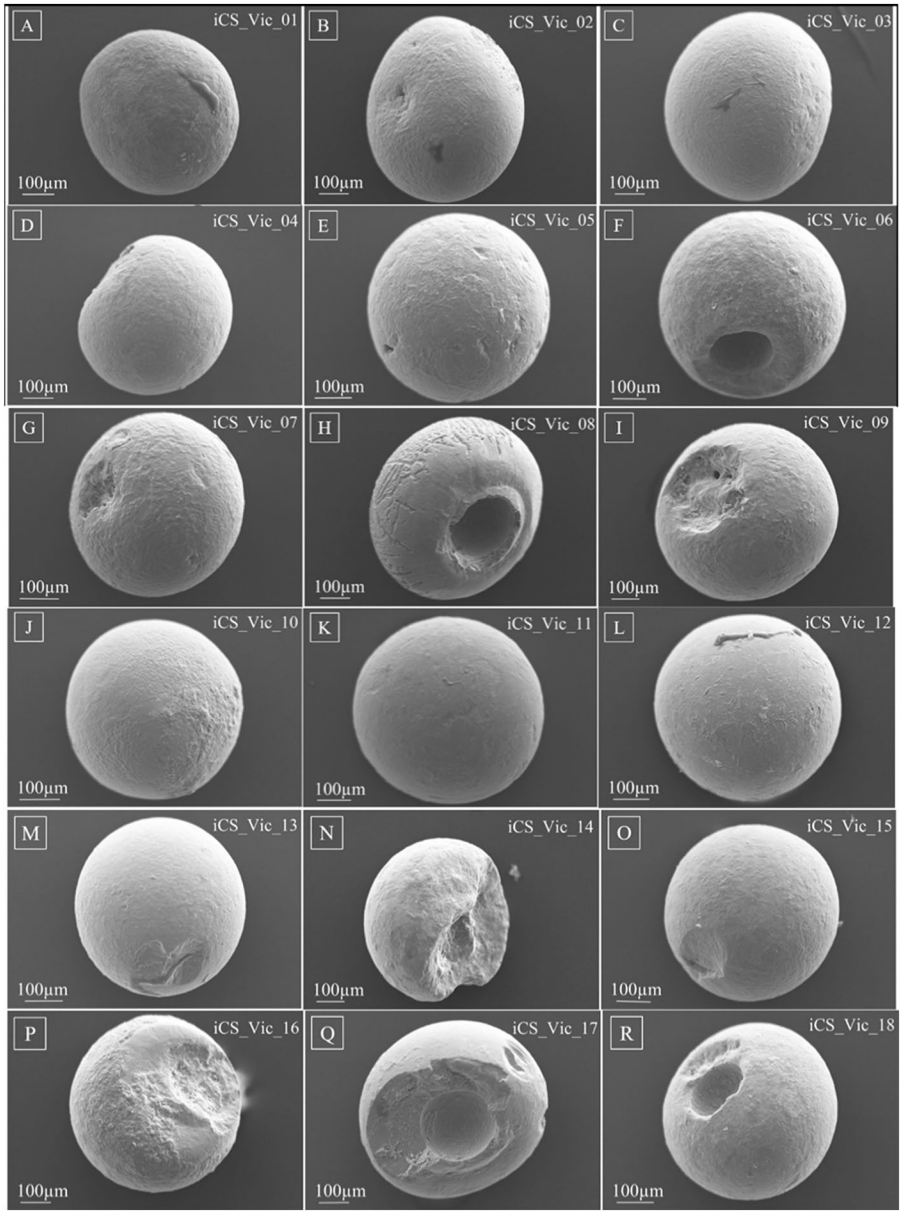

Figure 2. (a–r) Scanning electron images of the studied cosmic spherules (iCS_Vic _01...18; Table 2) from the Transantarctic Mountains collection. Some spheres show cavities at their surface indicating loss of residual metal beads during entry (f, h, q, r).

5. Discussion

5.1. Morphology and Density of the Studied Cosmic Spherules

All samples have spherical shapes indicative of melting during the atmospheric entry suggesting temperatures exceeding the melting point of Fe,Ni metal at ~1,550°C (Figures 2a–2r). A number of spherules have spherical voids that formed when residual Fe,Ni metal was lost from the surface of the leading side of the spheres during entry (Genge et al., 2008); prominent examples are shown in Figures 2f, 2h, 2n, 2q, and 2r. The typical density of the spherules is ~5.4 g cm^{-1} (Table 2) and is compatible with being mainly composed of a mixture of magnetite (5.2 g cm^{-1}) and wüstite (5.7 g cm^{-1}).

Table 5
List of the Oxygen Isotope Compositions of the Studied Cosmic Spherules

Identifier	$\delta^{17}O$ (‰)	1σ	$\delta^{18}O$ (‰)	1σ	$\Delta'^{17}O$ (‰)	1σ
iCS_Vic_01	25.19	0.20	48.01	0.37	−0.81	0.03
iCS_Vic_02	24.48	0.20	46.65	0.37	−0.74	0.03
iCS_Vic_03	20.40	0.20	38.80	0.37	−0.56	0.03
iCS_Vic_04	22.42	0.20	42.67	0.37	−0.64	0.03
iCS_Vic_05	24.43	0.20	46.55	0.37	−0.75	0.03
iCS_Vic_06	22.86	0.20	43.53	0.37	−0.62	0.03
iCS_Vic_07	24.21	0.20	46.13	0.37	−0.71	0.03
iCS_Vic_09	22.08	0.20	42.03	0.37	−0.66	0.03
iCS_Vic_10	24.61	0.20	46.90	0.37	−0.75	0.03
iCS_Vic_11	22.05	0.20	41.98	0.37	−0.61	0.03
iCS_Vic_12	23.30	0.20	44.38	0.37	−0.52	0.03
iCS_Vic_13	21.85	0.20	41.59	0.37	−0.57	0.03
iCS_Vic_14	20.65	0.20	39.27	0.37	−0.53	0.03
iCS_Vic_15	21.36	0.20	40.65	0.37	−0.59	0.03
iCS_Vic_16	21.43	0.20	40.79	0.37	−0.53	0.03
iCS_Vic_17	23.14	0.20	44.07	0.37	−0.66	0.03
iCS_Vic_18	21.85	0.20	41.58	0.37	−0.63	0.03

Note. The δ values are reported relative to VSMOW2. Errors are reported as 1σ SD.

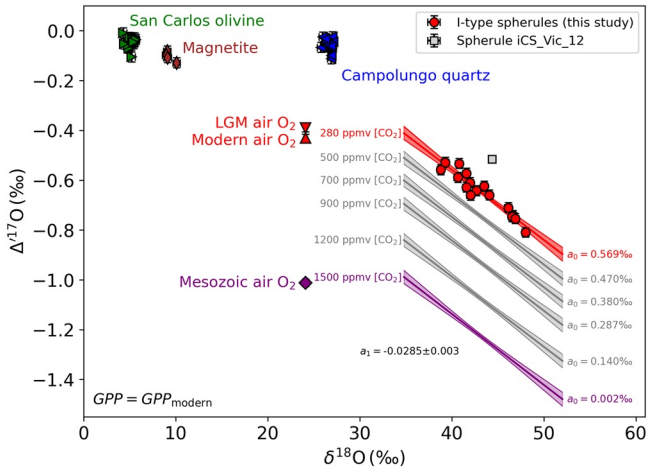

Figure 3. Plot of $\Delta'^{17}O$ versus- $\delta^{18}O$ of cosmic spherules and standards (San Carlos olivine [green-filled triangles], Campolungo quartz [blue-filled triangles], magnetite Mt_0701113 [brown-filled diamonds]) from this study. The data fall on a tight trend with a regression slope $a_1 = -0.0284$ (see Equation 6; excluding sample iCS_Vic_12 [light-gray-filled square]). The compositions of modern ($\Delta'^{17}O = -0.431$‰, red-filled triangle) and last glacial maximum (LGM, red-filled downward-pointing triangle) air O_2 is displayed. The composition of putative Mesozoic air O_2 at $[CO_2] = 1{,}500$ ppm (purple-filled diamond; Young et al., 2014) is shown for comparison (see Figure 1). Changes in $\Delta'^{17}O$ of air O_2 are transferred 1:1 to changes in $\Delta'^{17}O$ of the I-type cosmic spherule array (lines with corresponding $[CO_2]$ and intercepts a_0 are indicated along with the respective 1σ uncertainty intervals).

5.2. The Isotope Composition of I-Type Cosmic Spherules

Replacing the continuous flow mode (Pack et al., 2017) by dual inlet gas source mass spectrometry allowed reduction of the analytical uncertainty for $\Delta'^{17}O$ down to 0.02‰ (1σ SD).

The analyzed spherules fall on a tight trend in the $\Delta'^{17}O$ versus $\delta^{18}O$ space (Figure 3), which is approximated by linear regression (Equation 6).

$$\Delta'^{17}O = a_0 + a_1 \times \delta^{18}O \quad (6)$$

The regression slope through the spherule data (excluding outlier sample iCS_Vic_12) has an intercept of $a_0 = 0.57 \pm 0.13$‰ and a slope of $a_1 = -0.0285 \pm 0.003$. As the oxygen isotope composition of I-type cosmic spherules is controlled by i) fractionation during the oxidation and ii) fractionation during the evaporation (Pack et al., 2017), this slope cannot be attributed to a single fractionation process and hence is not confined by the theoretical limits for a particular fractionation process (e.g., Young et al., 2002). However, generally low θ values are expected for the kinetic fractionation during oxidation and for the kinetic fractionation during the evaporation, which is compatible with the observed slope in the $\Delta'^{17}O$ versus $\delta^{18}O$ space. The slope is a function of the atmospheric entry conditions (velocity, mass, and entry angle), which have likely not changed in the past. The intercept is coupled to the $\Delta'^{17}O$ of the atmosphere and is thus expected to vary.

All spherules show strong enrichment in heavy iron isotopes ($15 \leq \delta^{56}Fe \leq 33$‰; Table 6). This enrichment is compatible with

Table 6
Iron Isotope Composition of the Studied Cosmic Spherules

Identifier	δ^{56}Fe (‰)	1σ	δ^{57}Fe (‰)	1σ	Δ'^{56}Fe (‰)	1σ
iCS_Vic_01	31.73	0.07	47.36	0.07	−0.13	0.03
iCS_Vic_02 (1)	32.67	0.08	48.80	0.07	−0.15	0.03
iCS_Vic_02 (2)	32.47	0.07	48.54	0.07	−0.18	0.03
Mean	*32.29*	*0.04*	*48.23*	*0.04*	*−0.16*	*0.02*
iCS_Vic_02	32.57	0.07	48.67	0.05	−0.17	0.03
iCS_Vic_03	27.41	0.01	40.88	0.05	−0.12	0.03
iCS_Vic_03 (1)	27.42	0.08	40.85	0.07	−0.09	0.03
iCS_Vic_03 (2)	27.40	0.09	40.91	0.07	−0.15	0.03
Mean	*27.41*	*0.03*	*40.88*	*0.04*	*−0.12*	*0.02*
iCS_Vic_04	23.75	0.07	35.37	0.06	−0.09	0.03
iCS_Vic_05	28.88	0.08	43.08	0.07	−0.12	0.03
iCS_Vic_06	18.28	0.04	27.26	0.06	−0.12	0.03
iCS_Vic_07	28.14	0.03	42.06	0.06	−0.18	0.03
iCS_Vic_09	29.33	0.10	43.77	0.11	−0.14	0.03
iCS_Vic_10	26.39	0.07	39.26	0.06	−0.06	0.03
iCS_Vic_11	18.38	0.04	27.39	0.05	−0.11	0.03
iCS_Vic_12	14.89	0.04	22.27	0.06	−0.15	0.03
iCS_Vic_13	19.18	0.03	28.63	0.05	−0.14	0.03
iCS_Vic_14	15.88	0.07	23.66	0.07	−0.10	0.03
iCS_Vic_15	13.40	0.08	19.95	0.06	−0.08	0.03
iCS_Vic_16	19.19	0.04	28.68	0.05	−0.16	0.03
iCS_Vic_17	15.15	0.03	22.50	0.05	−0.05	0.03
iCS_Vic_18	19.79	0.03	29.50	0.05	−0.11	0.03
iCS_Vic_08	14.37	0.03	21.46	0.05	−0.13	0.03

Note. The data are reported relative to IRMM-04. Numbers in brackets indicate numbers for duplicate measurements of the same sphere.

observation from other studies (e.g., Davis et al., 1991; Engrand et al., 2005; Pack et al., 2017) and result of evaporation during the atmospheric entry. Using the fractionation factor of $\alpha_{evaporation} = 0.9816$ ($^{56}/^{54}$Fe) from experiments by J. Wang et al. (1994) and data from Dauphas et al. (2004) degrees of evaporation range from 52% to 83%. The Δ'^{56}Fe values are all negative (Figure 4), which is due to the iron isotope $\theta_{evaporation}$ that is lower than the high-T equilibrium fractionation value of 0.6780 (Young et al., 2002). Assuming that the incoming Fe,Ni metal had Δ'^{56}Fe equal to that of chondritic metal (δ^{56}Fe = 0.00‰, δ^{57}Fe = 0.01‰; K. Wang et al., 2013), a $\theta_{evaporation} = 0.6749$ is suggested by the data. Graham's law for Rayleigh-type of evaporation of Fe atoms would result in a slope of 0.6751 (Figure 4, dotted line) and Rayleigh-type evaporation of FeO would follow a slope of 0.6737 (Figure 4, dashed line). The cosmic spherule data can be well-explained by Rayleigh-type evaporation of Fe and/or FeO with no or negligible back-reaction between vapor and spherule. That is compatible with the entry conditions where the evaporated gas is immediately dragged away from the spherule so that no back-reaction can occur. The authors are not aware of any process in nature that follows Graham's law of isotope fractionation, but the fractionation observed in cosmic spherules seems to be a closed approximation for this fractionation mechanism.

Pack et al. (2017) combined the oxygen and iron isotope data to reconstruct the Δ'^{17}O of atmospheric O_2 at time when the spherule entered the atmosphere. The relation between oxygen and iron isotope

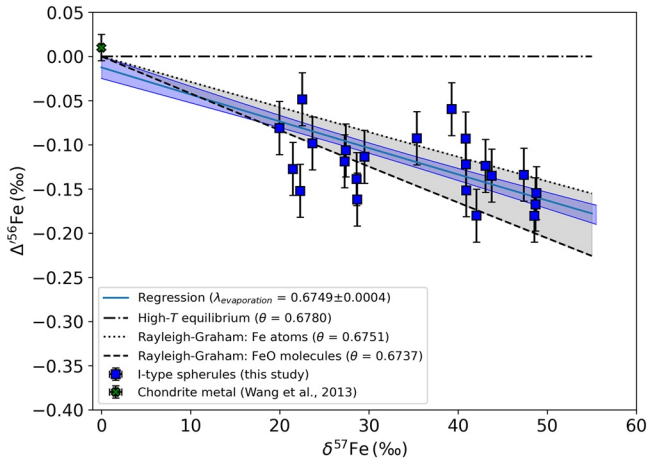

Figure 4. Plot of Δ'^{56}Fe versus δ^{57}Fe of cosmic spherules with clearly resolvable Δ'^{56}Fe variations. The composition of the original metal particles is assumed to be identical to that of chondritic metal (K. Wang et al., 2013). The evaporative enrichment follows a trend with $\lambda = 0.6749 \pm 0.0004$. The paths for Graham's law fractionation for pure Rayleigh-type evaporation processes of Fe atoms (dotted curve) and FeO (dashed curve) are shown for comparison along with the high-*T* approximation of equilibrium fractionation (Young et al., 2002; dashed-dotted line). The evaporation of cosmic spherules is well-explained by Rayleigh-type evaporation and Graham's law fractionation with little or no back-reaction.

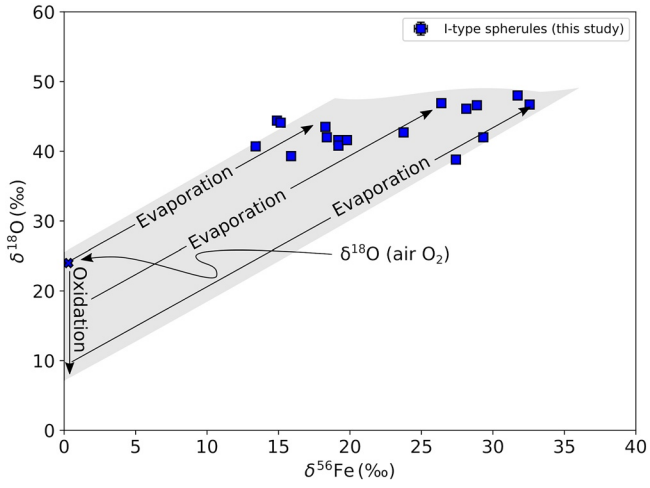

Figure 5. Plot of δ^{18}O versus δ^{56}Fe with the trajectories of the kinetic oxygen isotope fractionation during oxidation (Pack et al., 2017) and oxygen and iron isotope fractionation during evaporation (from J. Wang et al., 1994). The isotope composition of cosmic spherules could be described as a combination of the two fractionation effects in variable proportions. However, note the lack of correlation between O and Fe isotopes.

fractionation during evaporation was taken from the experiments by J. Wang et al. (1994). Adopting the two-step fractionation model by Pack et al. (2017), the extended oxygen and iron isotope data set from this study suggests that the fractionation during oxidation would vary between −15 and 0‰ (Figure 5).

The approach presented by Pack et al. (2017), however, was based on the experimental correlation between fractionation in δ^{18}O and fractionation in δ^{56}Fe from J. Wang et al. (1994). The data from this study, however, do not show such correlation between δ^{18}O and δ^{56}Fe (Figure 6a). Instead, variations in δ^{56}Fe, which are caused by evaporation, do not correlate much with variations in δ^{18}O. This indicates that back-reaction between Fe,Ni oxides and air is more pronounced for that for oxygen than for iron. This can be well-understood by the fact that air is rich in oxygen, but free of iron. The lack of a correlation between oxygen and iron isotope composition in cosmic spherules limits the applicability of the approach by Pack et al. (2017). While the δ^{56}Fe continuously increases during evaporation, δ^{18}O may reach a steady state between increase due to evaporation and equilibration with ambient air. The steady state may be at 46‰. Still, the relation between Δ'^{17}O and the degree of evaporation f (deduced from δ^{56}Fe; see Pack et al., 2017; Figure 6b) is compatible with some coupling between oxygen and iron isotopy even at high degrees of evaporation. The decreasing Δ'^{17}O with increasing f would then be explained by the low theta associated with kinetic fractionation during evaporation.

Instead of using combined oxygen and iron isotope data (Pack et al., 2017), we suggest here that the oxygen isotope data alone provide information about the Δ'^{17}O at time of the atmospheric entry of I-type cosmic spherules. The extended and improved data from this study show that the I-type spherules fall on a tight trend in the three-oxygen isotope space (Figure 3). As I-type spherules contain only atmospheric oxygen, changes in Δ'^{17}O of the atmosphere are transferred 1:1 to the intercept of the line defined by the spherules; the slope of that line is solely controlled by the entry conditions and hence assumed to be constant. The Δ'^{17}O of air O_2 can be calculated from the Δ'^{17}O and δ^{18}O values of an I-type cosmic spherule (Equation 6).

$$\Delta'^{17}O^{\text{air }O_2} = \Delta'^{17}O\text{spherule} - 0.0285 \cdot \delta^{18}O^{\text{spherule}} - 0.570‰ - 0.431‰ \quad (7)$$

For using Equation 6, Δ'^{17}O has to be defined as in Equation 1 with both, δ^{17}O and δ^{18}O on VSMOW scale, which we have anchored to San Carlos olivine with a $\Delta'^{17}O = -0.052‰$; a number based on studies that have analyzed both, San Carlos olivine and VSMOW2 water in the same laboratory (Pack et al., 2016; Sharp et al., 2016; Wostbrock et al., 2020). The term −0.431‰ is the composition of the modern atmosphere. For a proper paleo-CO_2 determination on fossil I-type spherules, a number of spherules should be analyzed and the average Δ'^{17}O of air O_2 should be taken as the value for the respective time interval.

From pure statistical analysis of the current data set of 16 spherules, a similar set of fossil I-type spherules would allow reconstruction of the corresponding air O_2 Δ'^{17}O better than 0.01‰. This transforms to a

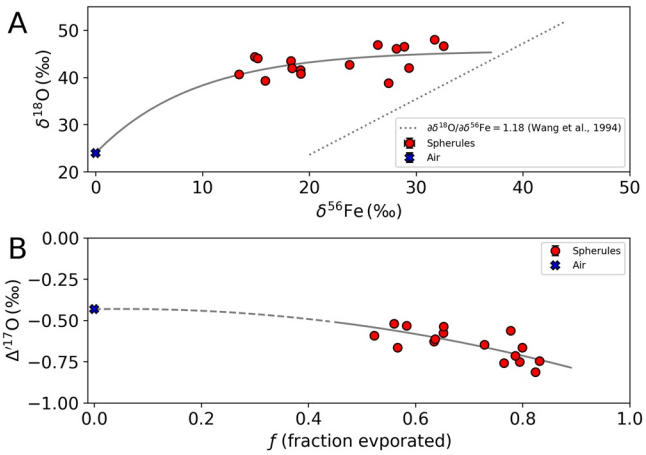

Figure 6. (a) Plot of $\delta^{18}O$ versus $\delta^{56}Fe$ of cosmic spherules from this study. The spherules do not show a linear correlation between $\delta^{18}O$ and $\delta^{56}Fe$ as observed by J. Wang et al. (1994; dotted line). The data suggest that with increasing evaporation, $\delta^{18}O$ rather reaches a steady state instead of continuously increasing. (b) Plot of $\Delta'^{17}O$ versus degree of evaporation (f). Higher degrees of evaporation (deduced from $\delta^{56}Fe$) are associated with lower $\Delta'^{17}O$. The composition ($\delta^{18}O$, $\Delta'^{17}O$) of air O_2 is shown for reference.

resolution of 25 ppm for $[CO_2]$ and 6% for GPP at $200 \leq [CO_2] \leq 1{,}500$ ppmv and 50% $GPP_{modern} \leq GPP \leq 150\%$ GPP_{modern}. The main challenge of this new paleo-CO_2-proxy is the state of preservation and the age distribution of I-type spherules in a sedimentary layer, and the analytical challenge related to the size of the spherules. All these three challenges can be addressed. The preservation state can be monitored by X-ray diffraction through the identification of wüstite and/or metal along with magnetite. Wüstite and metal are both unstable in the sedimentary environment and indicate a pristine nature of these materials. The absence of ferric oxides and hydroxides is further constraint for an unaltered state. Spherules may undergo sedimentary re-deposition, which could reduce the age resolution. Oxygen isotopic variability within the spherule populations (i.e., scatter around a trendline in the $\Delta'^{17}O$ vs. $\delta^{18}O$ diagram that significantly exceeds the analytical scatter) could indicate that the spherules arrived on Earth at times with marked different $\Delta'^{17}O$ of air O_2. A main challenge is the sizes of the spherules. Very small spherules are difficult to analyze by laser fluorination, but techniques suitable for small samples (e.g., ion microprobe) have a too large uncertainty in $\Delta'^{17}O$. Future technical developments, however, may well overcome this limitation.

Data Availability Statement

All oxygen and iron isotope data are available from the Göttingen Research Online data repository (https://doi.org/10.25625/ALRTAS).

Acknowledgments
We thank the three reviewers for their thorough and most helpful comments and suggestions, which led to a considerable improvement of the manuscript. The AE is thanked for his suggestions and manuscript handling. Open Access funding enabled and organized by Projekt DEAL.

References

Bao, H., Lyons, J. R., & Zhou, C. (2008). Triple oxygen isotope evidence for elevated CO_2 levels after a Neoproterozoic glaciation. *Nature*, *453*, 504–506.

Barkan, E., & Luz, B. (2005). High precision measurements of $^{17}O/^{16}O$ and $^{18}O/^{16}O$ ratios in H_2O. *Rapid Communications in Mass Spectrometry*, *19*, 3737–3742.

Barkan, E., & Luz, B. (2011). The relationships among the three stable isotopes of oxygen in air, seawater, and marine photosynthesis. *Rapid Communications in Mass Spectrometry*, *25*, 2367–2369.

Blunier, T., Barnett, B., Bender, M. L., & Hendricks, M. B. (2002). Biological oxygen productivity during the last 60,000 years from triple oxygen isotope measurements. *Global Biogeochemical Cycles*, *16*, 1–13. https://doi.org/10.1029/2001GB001460

Boering, K. A. (2004). Observations of the anomalous oxygen isotopic composition of carbon dioxide in the lower stratosphere and the flux of the anomaly to the troposphere. *Geophysical Research Letters*, *31*, L03109. https://doi.org/10.1029/2003GL018451

Brandon, M., Landais, A., Duchamp-Alphonse, S., Favre, V., Schmitz, L., Abrial, H., et al. (2020). Exceptionally high biosphere productivity at the beginning of Marine Isotopic Stage 11. *Nature Communications*, *11*, 1–10.

Cao, X., & Liu, Y. (2011). Equilibrium mass-dependent fractionation relationships for triple oxygen isotopes. *Geochimica et Cosmochimica Acta*, *75*, 7435–7445.

Chapligin, B., Meyer, H., Friedrichsen, H., Marent, A., Sohns, E., & Hubberten, H.-W. (2010). A high-performance, safer and semi-automated approach for the $\delta^{18}O$ analysis of diatom silica and new methods for removing exchangeable oxygen. *Rapid Communications in Mass Spectrometry*, *24*, 2655–2664.

Dauphas, N., Janney, P. E., Mendybaev, R. A., Wadhwa, M., Richter, F. M., Davis, A. M., et al. (2004). Chromatographic separation and multicollection-ICPMS analysis of iron. Investigating mass-dependent and -independent isotope effects. *Analytical Chemistry*, *76*, 5855–5863.

Davis, A. M., Clayton, R. N., Mayeda, T. K., & Brownlee, D. E. (1991). *Large mass fractionation of iron isotopes in cosmic spherules collected from deep-sea sediments*. Lunar and Planetary Science Conference, XXII, pp. 281–282.

Dole, M., Lane, G. A., Rudd, D. P., & Zaukelies, D. A. (1954). Isotopic composition of atmospheric oxygen and nitrogen. *Geochimica et Cosmochimica Acta*, *6*, 65–78.

Engrand, C., McKeegan, K. D., Leshin, L. A., Herzog, G. F., Schnabel, C., Nyquist, L. E., & Brownlee, D. E. (2005). Isotopic compositions of oxygen, iron, chromium, and nickel in cosmic spherules: Toward a better comprehension of atmospheric entry heating effects. *Geochimica et Cosmochimica Acta*, *69*, 5365–5385.

Folco, L., & Cordier, C. (2015). Micrometeorites. In M. R. Lee & H. Leroux (Eds.), *European mineralogical union notes in planetary mineralogy* (Vol. 15, pp. 253–297). The Mineralogical Society of Great Britain and Ireland.

Gehler, A., Gingerich, P. D., & Pack, A. (2016). Temperature and atmospheric CO_2 concentration estimates through the PETM using triple oxygen isotope analysis of mammalian bioapatite. *Proceedings of the National Academy of Sciences of the United States of America*, *113*, 7739–7744.

Genge, M. J. (2016). The origins of I-type spherules and the atmospheric entry of iron micrometeoroids. *Meteoritics & Planetary Science*, *51*, 1063–1081.
Genge, M. J., Engrand, C., Gounelle, M., & Taylor, S. (2008). The classification of micometeorites. *Meteoritics & Planetary Science*, *43*, 497–515.
Heard, A. W., Dauphas, N., Guilbaud, R., Rouxel, O. J., Butler, I. B., Nie, N. X., & Bekker, A. (2020). Triple iron isotope constraints on the role of ocean iron sinks in early atmospheric oxygenation. *Science*, *370*, 446–449.
Heidenreich, J. E., & Thiemens, M. H. (1986). A non-mass-dependent oxygen isotope effect in the production of ozone from molecular oxygen: The role of molecular symmetry in isotope chemistry. *The Journal of Chemical Physics*, *84*, 2129.
Kawagucci, S., Tsunogai, U., Kudo, S., Nakagawa, F., Honda, H., Aoki, S., et al. (2008). Long-term observation of mass-independent oxygen isotope anomaly in stratospheric CO_2. *Atmospheric Chemistry and Physics*, *8*, 6189–6197.
Krankowsky, D., Lämmerzahl, P., & Mauersberger, K. (2000). Isotopic measurements of stratospheric ozone. *Geophysical Research Letters*, *27*, 2593–2595.
Lämmerzahl, P. (2002). Oxygen isotope composition of stratospheric carbon dioxide. *Geophysical Research Letters*, *29*, 2426. https://doi.org/10.1029/2001GL014343
Luz, B., Barkan, E., Bender, M. L., Thiemens, M. H., & Boering, K. A. (1999). Triple-isotope composition of atmospheric oxygen as a tracer of biosphere productivity. *Nature*, *400*, 547–550.
Matsuhisa, Y., Goldsmith, J. R., & Clayton, R. N. (1978). Mechanisms of hydrothermal crystallization of quartz at 250°C and 15 kbar. *Geochimica et Cosmochimica Acta*, *42*, 173–182.
McKinney, C. R., McCrea, J. M., Epstein, S., Allen, H. A., & Urey, H. C. (1950). Improvements in mass spectrometers for the measurement of small differences in isotope abundance ratios. *Review of Scientific Instruments*, *21*, 724–730.
Miller, M. F., & Pack, A. (2021). Why measure ^{17}O? Historical perspective, triple-isotope systematics and selected applications. *Reviews in Mineralogy and Geochemistry*, *86*, 1–34.
Oeser, M., Weyer, S., Horn, I., & Schuth, S. (2014). High-precision Fe and Mg isotope ratios of silicate reference glasses determined in situ by femtosecond LA-MC-ICP-MS and by solution nebulization MC-ICP-MS. *Geostandards and Geoanalytical Research*, *38*, 311–328.
Pack, A. (2021). Isotopic traces of atmospheric O_2 in rocks, minerals, and melts. *Reviews in Mineralogy and Geochemistry*, *86*, 217–240.
Pack, A., Gehler, A., & Süssenberger, A. (2013). Exploring the usability of isotopically anomalous oxygen in bones and teeth as paleo-CO_2-barometer. *Geochimica et Cosmochimica Acta*, *102*, 306–317.
Pack, A., & Herwartz, D. (2014). The triple oxygen isotope composition of the Earth mantle and understanding $\Delta^{17}O$ variations in terrestrial rocks and minerals. *Earth and Planetary Science Letters*, *390*, 138–145.
Pack, A., Höweling, A., Hezel, D. C., Stefanak, M. T., Beck, A.-K., Peters, S. T. M., et al. (2017). Tracing the oxygen isotope composition of the upper Earth's atmosphere using cosmic spherules. *Nature Communications*, *8*, 15702.
Pack, A., Tanaka, R., Hering, M., Sengupta, S., Peters, S., & Nakamura, E. (2016). The oxygen isotope composition of San Carlos olivine on the VSMOW2-SLAP2 scale. *Rapid Communications in Mass Spectrometry*, *30*, 1495–1504.
Rochette, P., Folco, L., Suavet, C., van Ginneken, M., Gattacceca, J., Perchiazzi, N., et al. (2008). Micrometeorites from the Transantarctic Mountains. *Proceedings of the National Academy of Sciences of the United States of America*, *105*, 18206–18211.
Sharp, Z. D. (1990). A laser-based microanalytical method for the in situ determination of oxygen isotope ratios of silicates and oxides. *Geochimica et Cosmochimica Acta*, *54*, 1353–1357.
Sharp, Z. D., Gibbons, J. A., Maltsev, O., Atudorei, V., Pack, A., Sengupta, S., et al. (2016). A calibration of the triple oxygen isotope fractionation in the SiO_2–H_2O system and applications to natural samples. *Geochimica et Cosmochimica Acta*, *186*, 105–119.
Sharp, Z. D., & Wostbrock, J. A. G. (2021). Standardization for the triple oxygen isotope system: Waters, silicates, carbonates, air, and sulfates. *Reviews in Mineralogy and Geochemistry*, *86*, 179–196.
Suttle, M. D., & Folco, L. (2020). The extraterrestrial dust flux: Size distribution and mass contribution estimates inferred from the Transantarctic Mountains (TAM) micrometeorite collection. *Journal of Geophysical Research: Planets*, *125*, e2019JE006241. https://doi.org/10.1029/2019JE006241
Taylor, S., Lever, J. H., & Harvey, R. P. (1998). Accretion rate of cosmic spherules measured at the South Pole. *Nature*, *392*, 899–903.
Taylor, S., Lever, J. H., & Harvey, R. P. (2000). Numbers, types, and compositions of an unbiased collection of cosmic spherules. *Meteoritics & Planetary Science*, *35*, 651–666.
Thiemens, M. H., Chakraborty, S., & Dominguez, G. (2012). The physical chemistry of mass-independent isotope effects and their observation in nature. *Annual Review of Physical Chemistry*, *63*, 155–177.
Thiemens, M. H., & Heidenreich, J. E. (1983). The mass-independent fractionation of oxygen: A novel isotope effect and its possible cosmochemical implications. *Science*, *219*, 1073–1075.
Thiemens, M. H., Jackson, T., Zipf, E. C., Erdman, P. W., & van Egmond, C. (1995). Carbon dioxide and oxygen isotope anomalies in the mesosphere and stratosphere. *Science*, *270*, 969–972.
Wang, J., Davis, A. M., Clayton, R. N., & Mayeda, T. K. (1994). *Kinetic isotopic fractionation during the evaporation of the iron oxide from liquid state (abstract)*. Lunar and Planetary Science Conference XXV.
Wang, K., Moynier, F., Barrat, J. -A., Zanda, B., Paniello, R. C., & Savage, P. S. (2013). Homogeneous distribution of Fe isotopes in the early solar nebula. *Meteoritics & Planetary Science*, *48*, 354–364.
Weyer, S., & Schwieters, J. B. (2003). High precision Fe isotope measurements with high mass resolution MC-ICPMS. *International Journal of Mass Spectrometry*, *226*, 355–368.
Weyrauch, M., Oeser, M., Brüske, A., & Weyer, S. (2017). In situ high-precision Ni isotope analysis of metals by femtosecond-LA-MC-ICP-MS. *Journal of Analytical Atomic Spectrometry*, *32*, 1312–1319.
Wostbrock, J. A. G., Cano, E. J., & Sharp, Z. D. (2020). An internally consistent triple oxygen isotope calibration of standards for silicates, carbonates and air relative to VSMOW2 and SLAP2. *Chemical Geology*, *533*, 119432.
Yeung, L. Y., Young, E. D., & Schauble, E. A. (2012). Measurements of $^{18}O^{18}O$ and $^{17}O^{18}O$ in the atmosphere and the role of isotope-exchange reactions. *Journal of Geophysical Research*, *117*, D18306. https://doi.org/10.1029/2012JD017992
Young, E. D., Galy, A., & Nagahara, H. (2002). Kinetic and equilibrium mass-dependent isotope fractionation laws in nature and their geochemical and cosmochemical significance. *Geochimica et Cosmochimica Acta*, *66*, 1095–1104.
Young, E. D., Yeung, L. Y., & Kohl, I. E. (2014). On the $\Delta^{17}O$ budget of atmospheric O_2. *Geochimica et Cosmochimica Acta*, *135*, 102–125.